

www.acsami.org Research Article

Ion—Solvent Interplay in Concentrated Electrolytes Enables Subzero Temperature Li-Ion Battery Operations

Soohwan Kim, Bumjoon Seo, Hari Vignesh Ramasamy, Zhongxia Shang, Haiyan Wang, Brett M. Savoie,* and Vilas G. Pol*



Cite This: ACS Appl. Mater. Interfaces 2022, 14, 41934–41944



ACCESS I Metrics & More Article Recommendations Supporting Information Enhanced subzero performance 200 Capacity (mAh g⁻⁷ Intensity (a.u.) Thin SEI FSI^{*} 100 **HSCE** Graphite 700 720 740 760 780 NCM622 | | Graphite Raman shift (cm⁻¹) 10 20 30 Cycle number 40 AGG dominant Li+ solvation structure

ABSTRACT: Despite the essential role of ethylene carbonate (EC) in solid electrolyte interphase (SEI) formation, the high Li⁺ desolvation barrier and melting point (36 °C) of EC impede lithium-ion battery operation at low temperatures and induce sluggish Li⁺ reaction kinetics. Here, we demonstrate an EC-free high salt concentration electrolyte (HSCE) composed of lithium bis(fluorosulfonyl)imide salt and tetrahydrofuran solvent with enhanced subzero temperature operation originating from unusually rapid low-temperature Li⁺ transport. Experimental and theoretical characterizations reveal the dominance of intra-aggregate ion transport in the HSCE that enables efficient low-temperature transport by increasing the exchange rate of solvating counterions relative to that of solvent molecules. This electrolyte also produces a <5 nm thick anion-derived LiF-rich SEI layer with excellent graphite electrode compatibility and electrochemical performance at subzero temperature in half-cells. Full cells based on LiNi_{0.6}Co_{0.2}Mn_{0.2}O₂llgraphite with tailored HSCE electrolytes outperform state-of-the-art cells comprising conventional EC electrolytes during charge—discharge operation at an extreme temperature of -40 °C. These results demonstrate the opportunities for creating intrinsically robust low-temperature Li⁺ technology.

KEYWORDS: lithium, ion pairs, interfacial chemistries, high concentration electrolytes, low temperatures

■ INTRODUCTION

Lithium-ion batteries (LIBs) are a focal point of economic growth worldwide due to their high energy and power densities, low self-discharge rate, and widespread application, including for portable electronics and electric vehicles. 1-4 Nevertheless, the meager performance of conventional LIB technologies at low temperatures remains a barrier to submarines, unmanned aerial vehicles, and space exploration applications.^{3,4} In particular, prevailing carbonate electrolytes are unsuited to low-temperature LIB operation due to (i) low ionic conductivity, (ii) limited low-temperature salt solubility, (iii) high Li⁺ desolvation barriers at the solid electrolyte interphase (SEI), and (iv) the high solvent melting point. To partially offset these issues, state-of-the-art LIBs rely on secondary heating systems for low-temperature operation, while still relying on carbonate electrolytes due to their high optimization, especially with respect to SEI formation.^{3,8,9} This costly and limited solution suggests that the carbonate

electrolyte paradigm ultimately needs to be abandoned for alternative solvent and salt combinations that are designed specifically for low-temperature operation.^{3,4}

High salt concentration electrolytes (HSCEs) are a potentially promising replacement for carbonates that have recently been studied by several groups due to their distinct ion transport and SEI formation behaviors. ^{10–12} In these systems, increasing the salt concentration promotes speciation without salt precipitation or complete suppression of the Li⁺ conductivity. ^{10,11} In addition to the solvent-separated ion pairs

Received: May 25, 2022 Accepted: September 4, 2022 Published: September 9, 2022





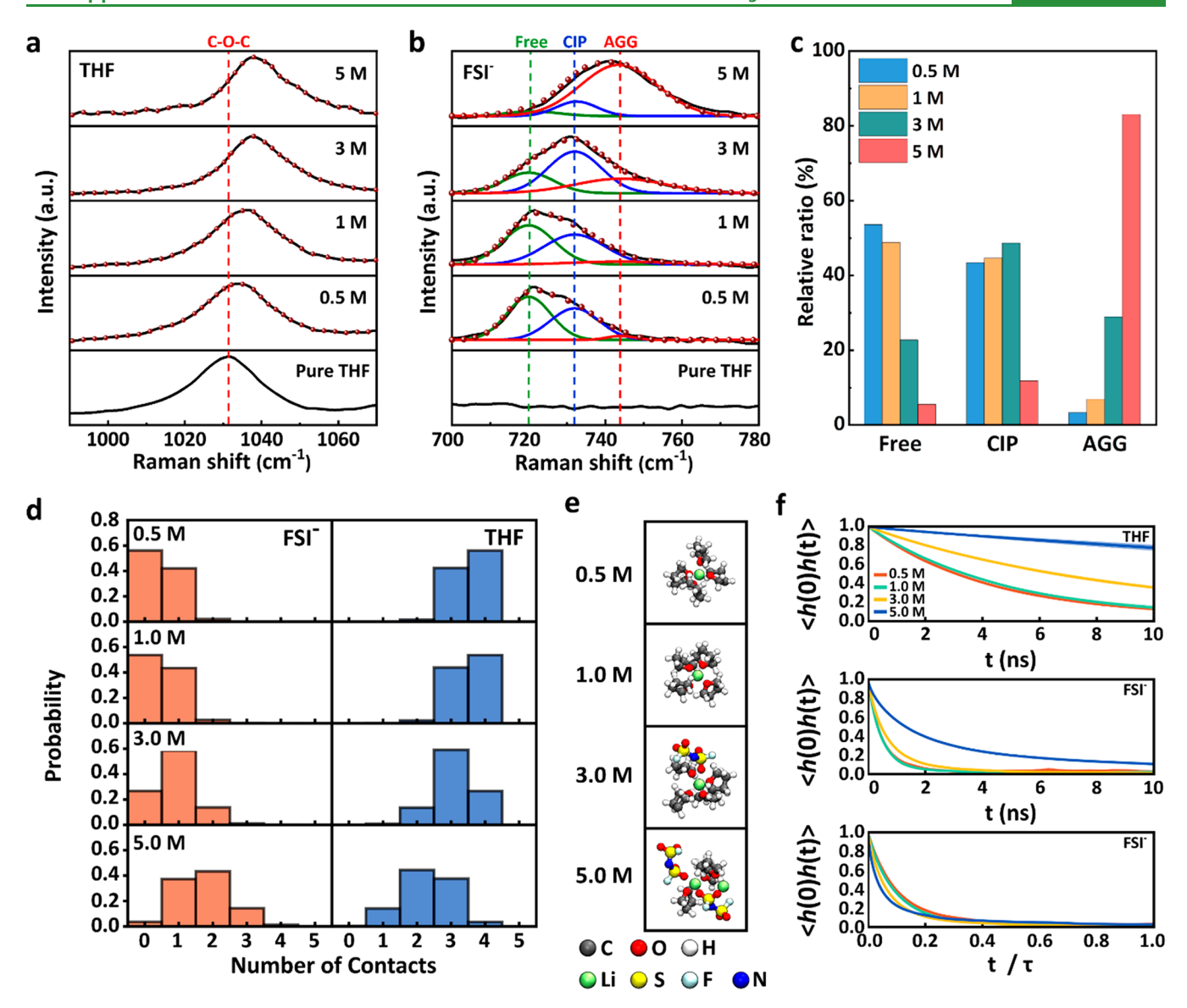


Figure 1. Solvation structure depending on salt concentration. (a) Raman spectra of electrolytes in the ranges 990–1070 cm⁻¹ (C–O–C vibrational mode of THF) and (b) 700–780 cm⁻¹ (S–N–S vibrational mode of FSI⁻). (c) Distribution of the Li⁺ solvation structures based on the Raman spectra. (d) Number of contacts between FSI⁻–Li⁺ and THF–Li⁺ in the first solvation shell histogrammed across the simulations. (e) Coordination structures of Li⁺ reflecting the mode solvation structure at each concentration. (f) (top, middle) Contact durations for the Li⁺ and the dominant binding oxygens. (bottom) Contact durations for the FSI⁻ oxygens as a function of the simulation time divided by the decay constant of the solvent contact durations.

and contact ion pairs (CIPs) that also occur in dilute electrolytes, the presence of larger aggregates (AGGs) of ions with potentially dynamic membership has a significant role in the physicochemical and interfacial properties of HSCEs. ¹³ The participation of anions in Li⁺ solvation through these AGGs also leads to an increase in the effective electron affinity of the anions and the generation of anion decomposition products in the SEI. ^{10–12,14} This distinct SEI structure is reported to have several promising properties, including robustness during the LIBs operation, low interfacial resistance, and fast ion transfer kinetics. ^{10,11,15,16} These SEI attributes correlate with improved LIB performance with respect to energy density, cycling lifetime, and charging rates. ^{11,16–19}

A major attraction of the HSCE paradigm is that it dramatically broadens the design space of possible solvents by decoupling the SEI properties from the solvent. Here

this aspect of HSCEs is leveraged to optimize a solvent system for low-temperature LIB operation while retaining a robust SEI. A novel HSCE is described that is based on a mixture of tetrahydrofuran (THF) solvent and lithium bis-(fluorosulfonyl)imide (LiFSI) salt. THF as a solvent has physical properties that are beneficial for developing an HSCE aimed at low-temperature operation, such as low melting point (-109 °C), low viscosity, and a sufficient dielectric constant for dissolving lithium salts. 8,22,23 Furthermore, the chemical stability of THF is superior to other ether solvents with similar physical properties such as 1,3-dioxolane, which is prone to ring-opening and polymerization. 24,25 THF-based electrolytes have been investigated for low-temperature applications with titanium disulfide electrodes; however, application to graphitic anodes has remained limited by the overlapped reduction potential (0.01-0.25 V vs Li/Li⁺) with that of THF (0.0-0.3 V vs Li/Li^+). 22,23,26,27 Because of the absence of a robust SEI,

repeated THF reduction occurs within the potential window at typical salt concentration and thereby causes reversible capacity loss. The distinct anion-derived SEI of HSCE provides a potential means of circumventing this limitation. LiFSI salt for the HSCE also provides additional advantages for lowtemperature LIB operation compared to other lithium salts like lithium bis(trifluoromethanesulfonyl)imide (LiTFSI) and lithium hexafluorophosphate (LiPF₆). For example, the larger positive charge on the sulfur atoms and the smaller polarizability of FSI compared to those of TFSI induce weak interaction between Li⁺ and FSI^{-.28,29} It can minimize viscosity at high concentrations and results in higher ionic conductivity of LiFSI than that of LiPF₆ and LiTFSI. 18,30 FSI decomposition also creates a more stable SEI than PF₆⁻ or TFSI⁻ decomposition in the HSCEs. 10,11 This SEI is rich in inorganic compounds that effectively suppress solvent decomposition and conduce facile Li^+ transfer, including LiF and, to a lesser degree, Li_2O , Li_2S , and Li_3N . $^{15,31-33}$

In this work, we demonstrate a series of THF:LiFSI electrolyte formulations with unique solvation and SEI structures that provide an extended subzero temperature window for repeated charge-discharge cycling of LIBs. Experimental and theoretical analyses of these electrolytes reveal an AGG-dominant Li⁺ solvation structure within which Li⁺ transport is facilitated at high salt concentrations. Cycling these electrolytes in graphitic half-cells produced thin anionderived SEI layers enriched with LiF and other inorganic species. The AGG-rich solvation structure and SEI layer showed enhanced electrochemical performance for graphite half-cells at both room and subzero temperatures. Evaluation of Li⁺ kinetics by electrochemical methods reinforced the notion that the enhancement can be attributed to the kinetically favorable solvation and SEI structure along with the low melting point of THF solvent. Moreover, the enhanced low-temperature charge-discharge performance was effective for the $LiNi_{0.6}Co_{0.2}Mn_{0.2}O_2$ (NCM622)||graphite full cells as retaining 80% (at -20 °C) and 43% (at -40 °C) of the room temperature capacity.

RESULTS AND DISCUSSION

Experimental and Theoretical Analysis of Solvation Structures. The solvation structure of THF:LiFSI electrolytes at various lithium salt concentrations was investigated by Raman spectroscopy (Figure 1a). The peaks appearing at 990–1070 cm⁻¹ denote the C–O–C vibrational mode (1031 cm⁻¹) of the THF solvent.^{34,35} As the salt concentration is increased from 0 to 5 M, there is a gradual blue shift in this peak position caused by Li⁺-solvent coordination that shortens the C-O bond of the THF.³⁶ Figure 1b shows the Raman spectra between 700 and 780 cm⁻¹, corresponding to the S-N-S vibrational mode of FSI⁻³⁷ The peaks located at 720, 732, and 744 cm⁻¹ represent the free FSI⁻ (noncoordinated FSI⁻), CIPs (FSI⁻ coordinating with one Li⁺), and AGGs (FSI⁻ coordinating with two or more Li⁺), respectively. 17,37,38 With the increasing salt concentration from 0.5 to 5 M, the peaks representing noncoordinated FSI- decrease, whereas the peaks associated with CIPs and AGGs increase. These results indicate that the FSI participation in Li+ solvation increases with concentration, finally resulting in most FSI⁻ coordinating with Li⁺ as AGGs at 5 M (Figure 1c).

To characterize the structural and dynamic changes to the Li⁺ solvation structure that accompany increasing salt concentration, molecular dynamics (MD) simulations were

performed on THF:LiFSI electrolytes with varying salt concentration. The distributions of atomistic solvation structures were extracted from these simulations by histogramming the number of solvent molecules and anions within the first solvation shell of Li⁺ (Figure 1d). At 0.5 M (the lowest investigated concentration), the mode Li⁺ solvation shell was composed exclusively of THF molecules; ~40% of the structures could be classified as CIPs, but only ~2% of configurations exhibit multiple FSI- within the solvation structure. As the concentration increases, the THF molecules are displaced by FSI⁻ in the solvation shell. At a concentration of 3 M, the mode solvation structure is a CIP. At 5 M concentration, the mode solvation structure involves two or more anions constituting an AGG. This progression is clearly visualized in atomistic snapshots of the mode solvation structure drawn from the simulations at each concentration (Figure 1e). These observations are remarkably consistent with the progression from a mixture of free ions and CIPs at low concentrations to AGGs observed by Raman spectra. The radial distribution functions in Figure S2 show that the oxygen atoms within THF and FSI- drive the interaction with Li+. A sensitivity analysis was also performed to confirm that the qualitative conclusions of this analysis were unaffected by the specific values used to parse these histograms (Figure S3). The MD results also predict that there is a relatively broad distribution of anions in the solvation structure at high salt concentrations, which suggests that these anions may be relatively more labile than those involved in the relatively narrow CIP distributions observed at low concentration.

To investigate this hypothesis, the rate of exchange of solvent molecules and counterions in the Li⁺ solvation shell was calculated at each concentration (Figure 1f). These were calculated by defining a contact indicator function, h_{ii} , between Li+ and the oxygens in THF and FSI-, respectively, that returned one (zero) when it was within (without) the solvation shell. The contact duration, $\langle h_{ii}(0)h_{ii}(t)\rangle$, is the autocorrelation decay of this indicator function and provides a measure of the exchange rate of each species, under the assumption that a given species was initially within the solvation shell (Figure 1f).³⁹ For both THF and FSI⁻, the contact duration increases with the concentration, which is a trivial manifestation of the increasing solution viscosity. To measure the relative rate of the anion exchange to the solvent exchange, the FSI- contact durations were normalized by the decay constants of the THF solvent contact durations at each concentration. The autocorrelation decay as a function of this unitless time represents lability—the ability of the cations to exchange anions within the solvation shell compared to the exchange of coordinating solvent molecules. By this measure, the relative rate of anion exchange increases while that of solvent exchange decreases. This scenario is indicative of relatively facile transport of the anions within AGGs at high concentrations compared with relatively slow CIP exchange at low salt concentrations. This mechanism is also consistent with the experimental observation of increased Li⁺ transference numbers at higher salt concentrations.⁴⁰

Favorable SEI Layer Structure. Transmission electron microscopy (TEM) images provided the morphology of SEI layer on the surface of cycled graphite electrode particles in conventional electrolyte (CVE, 1 M LiPF₆ EC/DEC (1:1, v/v)) and high salt concentration electrolyte (HSCE, 5 M LiFSI THF). High-resolution TEM (HRTEM) shows 8–12 nm thick SEI layer covering the graphite electrode particles after

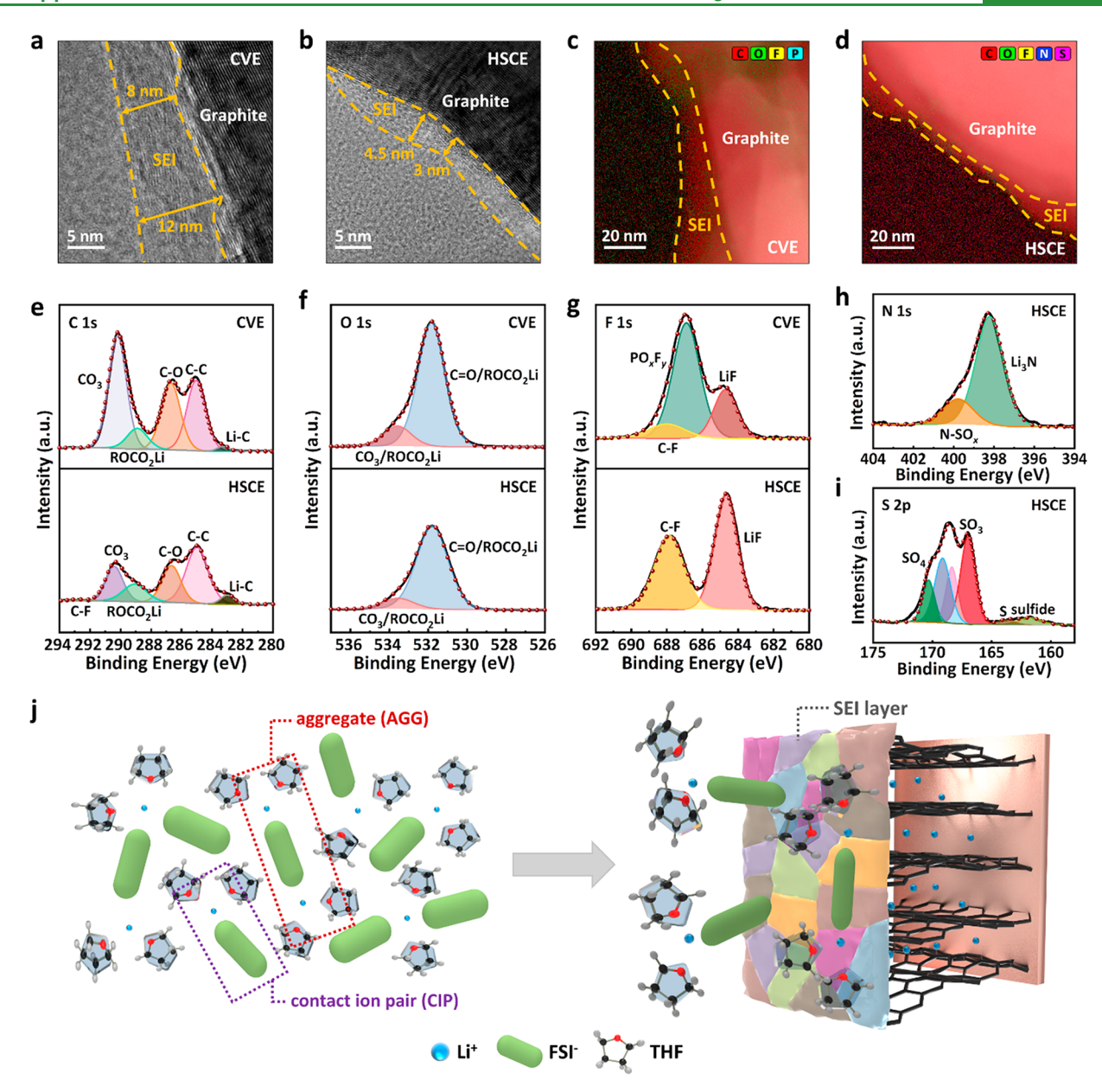


Figure 2. SEI morphology and chemistry arising from unique solvation structure. HRTEM images of the cycled graphite electrode particles in (a) CVE and (b) HSCE. Overlapped HAADF and EDS images of the cycled graphite electrode particles in (c) CVE and (d) HSCE. (e) C 1s, (f) O 1s, (g) F 1s, (h) N 1s, and (i) S 2p XPS spectra for the cycled graphite electrodes surface. (j) Schematic illustration of the solvation structure and SEI layer on the graphite electrode surface.

CVE cycling (Figures 2a and S5a) versus a much thinner SEI layer of 3–4.5 nm after HSCE cycling (Figures 2b and S5b). This characteristic difference in SEI layer is consistent with thin SEI layers observed in other HSCEs. Lenergy dispersive X-ray spectroscopy (EDS) atomic fraction mapping obtained under high angle annular dark field (HAADF) corroborated thin SEI layer formation with the HSCE (Figures 2c,d and S6). Only carbon and oxygen signals are apparent in the EDS atomic fraction mapping images due to dominance of these elements within the EDS penetration depth (Figures S7–S9). The EDS analysis generally provides an average composition of hundreds of nanometers to a few micrometers of samples, so it may be hard to differentiate other minor elements at the top few nanometers of the SEI. Nevertheless, strong oxygen signals at the graphite surface can reveal the SEI

thickness difference between the CVE and HSCE which is consistent with the HRTEM images.

X-ray photoelectron spectroscopy (XPS) analysis provides additional details for surface information, related to the SEI composition from the distinct electrolytes. The C 1s and O 1s spectra show similar peak positions for both electrolytes (Figure 2e,f). The atomic ratio and peak area ratio for organic species (C–O, ROCO₂Li, and CO₃) decreased in the HSCE for both C 1s and O 1s spectra (Tables S1 and S2), which suggests suppressed solvent decomposition on the surface compared to that of the CVE. In the F 1s spectra, an increased atomic ratio and the relatively higher content of LiF in the HSCE confirm that FSI⁻ decomposition drives SEI formation at the graphite electrode (Figure 2g, Tables S1 and S2). As discussed later in the context of electrochemical testing, low concentration formulations of the electrolyte do not exhibit

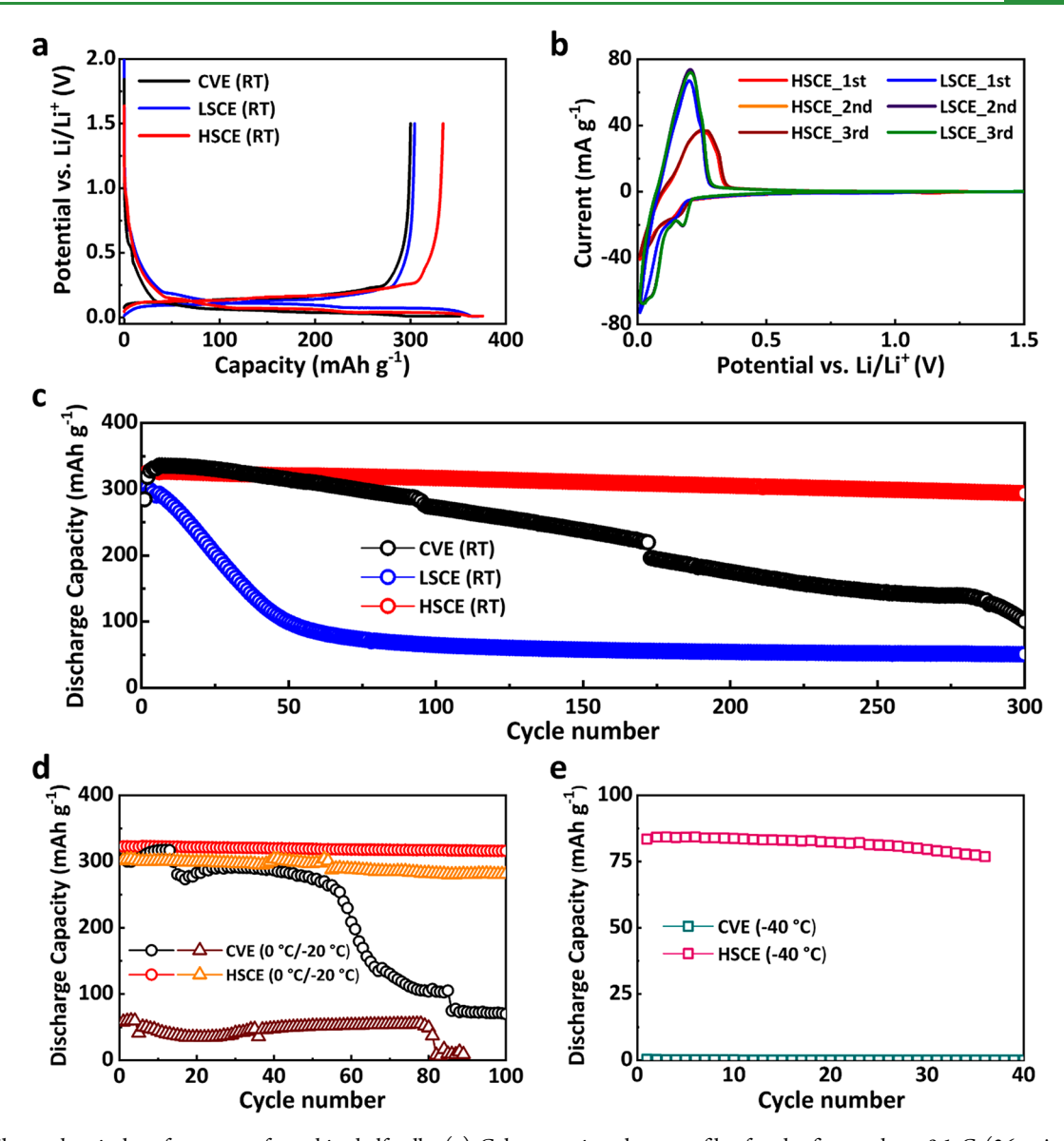


Figure 3. Electrochemical performance of graphite half-cells. (a) Galvanostatic voltage profiles for the first cycle at 0.1 C (36 mA g^{-1}) at room temperature (RT). (b) Cyclic voltammetry curves of graphite electrodes in HSCE and LSCE. (c) Cycling performance at 0.5 C (186 mA g^{-1}) and RT. (d) Low-temperature cycling performance at 0, -20, and (e) -40 °C.

robust SEI formation, supporting the hypothesis that this behavior relates to the unique solvation structure of the HSCE. The N 1s and S 2p spectra of the HSCE also show formation of other inorganic species from the FSI⁻ decomposition, including Li₃N and Li₂S, which are absent in the spectra for the CVE (Figures 2h,i and S10). Overall, the XPS spectra suggest that FSI⁻ decomposition from the HSCE resulted in an SEI layer containing inorganic species with larger amounts of LiF, whereas organic species mainly comprises the CVE SEI.

Figure 2j summarizes the interplay of ion solvation structure and favorable SEI properties occurring on the graphitic anode surface for the HSCE. The key feature of the HSCE is the extensive coordination of FSI⁻ around the Li⁺ in the form of AGGs, as confirmed by Raman spectroscopy and MD simulations. The dominance of AGG structures is known to substitute the solvent molecules with anions in the LUMO of the electrolyte, which in turn facilitates the decomposition of anions instead of solvent molecules.¹⁰⁻¹² Consequently, these effects successfully produced a thinner and anion-derived SEI

layer composed of rich LiF with other inorganic compounds such as Li₂O, Li₂S, and Li₃N. The thin SEI layer can give lower resistance for Li⁺ diffusion and electron transfer. EIs rich in LiF and other inorganic compounds also exhibit improved stability and rapid reaction kinetics at the electrolyte—electrode interfacial region. 15,31,32,38

Compatibility of the HSCE with the Graphite Electrode. To confirm the compatibility of the HSCE in LIB, electrochemical tests were performed at room temperature through galvanostatic cycling and cyclic voltammetry. The first cycle voltage profile of the graphite half-cells presents reversible Li⁺ reactions irrespective of the electrolytes used (Figure 3a). The graphite electrode in the CVE showed highly reversible Li⁺ intercalation/deintercalation with a small peak around 0.55 V during intercalation indicating solvent decomposition and the corresponding SEI layer formation (Figure S11a). However, there are no evident peaks around 0.55 V for the graphite electrodes in the THF-based low salt concentration electrolyte (LSCE, 1 M LiFSI in THF) and

HSCE, which revealed different electrolyte decomposition behavior in them. Nonetheless, they showed stable chargedischarge behavior with the graphite electrodes at the first cycle with three voltage plateaus between 0.01 and 0.25 V. These plateaus indicate that both the LSCE and HSCE performed as well as the CVE at the first cycle through three different stages of the Li⁺ intercalation process (Figure S11b).²⁶

However, the distinctions between the LSCE and HSCE are apparent in the cyclic voltammograms of the graphite electrodes (Figure 3b). A new peak occurred around 0.05 V during a cathodic scan in the curves of the LSCE after the first cycle (Figures S11c and S12a). Considering ether decomposes at 0.0-0.3 V,²⁷ this peak is ascribed to the decomposition of THF due to abundant noncoordinated THF molecules at low concentrations. This peak appeared in all subsequent cycles, indicating continuous consumption of the solvent and lack of a robust SEI, which eventually can lead to reversible capacity loss.^{8,30} Unlike the LSCE, the overlapped redox curves for the HSCE demonstrated excellent reversibility of Li+ reactions (Figure S12). The HSCE also showed a small peak at 1.14 V during a cathodic scan on the first cycle that indicated FSIdecomposition to form the SEI layer, 26,38 whereas solvent decomposition occurred in the LSCE (0.05 V) and CVE (0.6 V) (Figures S11c,d and S12).45 The effects of these distinct SEIs were evident in long-term cycling tests. The discharge capacities of the graphite electrode in the LSCE continuously decayed after the first cycle and reached 30% of initial capacity within 60 cycles (Figures 3c and S13a). In contrast, the graphite electrodes in the CVE and HSCE showed stable performance over 100 cycles with stable Coulombic efficiencies (CE, discharge capacity/charge capacity %) (Figures 3c and S13b-d). Moreover, the electrode in the HSCE maintained 90% of capacity retention over 300 cycles (Figures 3c and

The above results showed that a THF-based electrolyte with low salt concentration cannot create a robust SEI layer and causes continuous solvent decomposition, which resulted in the repetitive loss of reversible capacity. 46 However, the HSCE enabled the graphite electrode to operate stably and even achieved superiority over the CVE regarding long-term cycling performance due to the modified Li+ solvation structure and resultant thinner but robust anion-derived SEI layer. 10-12

Enhanced Performance at Subzero Temperature. In addition to the great compatibility with the graphite electrode, the developed HSCE enhanced the performance of cells at extreme conditions. The subzero temperature cycling tests of the graphite electrodes in different electrolytes revealed the enhanced electrochemical performance of the HSCE at all temperatures. At 0 °C, the discharge capacity of the graphite electrode with the HSCE (323 mAh g⁻¹) was almost the same as the capacity at room temperature and maintained over 100 cycles (Figure 3d), which is significant. On the other hand, the graphite electrode using the CVE did not show comparable performance and capacity dropped fast after 50 cycles. Furthermore, even at -20 °C, the graphite electrode using the HSCE could deliver a capacity of over 300 mAh g⁻¹ whereas only 59 mAh g⁻¹ capacity was delivered and faded further in the CVE (Figure 3d). As the temperature dropped to -40 °C, the graphite electrode using the HSCE was still able to deliver 84 mAh g⁻¹ (Figure 3e). Although the capacity at -40 °C was lower than that of 0 or −20 °C, its performance was improved compared with the graphite electrode in the

CVE, which has negligible electrochemical energy output (Figure S14). The low melting point of THF broadened the operating temperature window and led to the enhancement in electrochemical performance.

To find the source of the improved low-temperature performance of the HSCE besides the low melting point of THF solvent, we characterized bulk electrolyte transport properties through experimental methods (Table 1). Ob-

Table 1. Bulk Electrolyte Transport Properties

		conductivity (mS cm ⁻¹)			
electrolyte	viscosity (cP) (25 °C)	−20 °C	0 °C	30 °C	$t_{\mathrm{Li}^{^{+}}}$
CVE	5.04	1.85	3.42	6.52	0.359
HSCE	33.7	1.00	1.87	3.82	0.535

viously, the HSCE shows a higher viscosity of 33.7 cP than the viscosity of the CVE (5.04 cP) because of the higher number of ion pairs and ion clusters formed at high concentrations (Figure S15). Regardless, the developed HSCE exhibits an enhanced electrochemical performance decoupled from the high viscosity because of the hopping-type Li⁺ transport mechanisms. 10-12 The ion motions with these different types of mechanism compared to that of the conventional vehicletype mechanisms enable efficient Li⁺ transport despite the high viscosity. With regard to ionic conductivities of the electrolytes, the CVE exhibits higher values over a wide temperature range (-20 to 40 °C) than those of the HSCE (Figure S16), which is due to the decrease in absolute mobility of the ions. 47 However, the high Li⁺ transference number (t_{Li}^+) in the HSCE corroborates that the inferior ionic conductivity does not indicate degradation of Li⁺ transport in the HSCE (Figure S17 and Table S3). Therefore, the experimental results show that the HSCE provides efficient Li+ transport properties as indicated by the MD simulation. This is beneficial for LIB performance considering that energy densities and rate capabilities of the LIBs are predominantly involved in Li⁺ transfer rather than anion transfer. 48,49

Li⁺ kinetics at the interfacial region and bulk graphite electrodes was identified electrochemically for further investigation. Temperature-dependent electrochemical impedance spectroscopy (EIS) shows enhanced Li+ transport kinetics at the interfacial region of the graphite electrode in the HSCE. In the Nyquist plots, the high-frequency region represents Li+ transport through the SEI layer, and the mid-frequency region indicates the Li⁺ desolvation process (charge transfer at Li⁺ intercalation voltage) (Figure 4a,b).^{5,50} The resistance values are calculated by fitting the Nyquist plot using an equivalent circuit (Table S4). Arrhenius plots from these figures and resistance values provide the activation energies of Li+ transport at the interfacial region (Figure 4c,d). The HSCE shows reduced energy barriers for Li⁺ transport through SEI layer ($E_{a,SEI} = 27.5 \text{ kJ mol}^{-1}$) and Li⁺ desolvation ($E_{a,ct} = 40.3$ kJ mol⁻¹) compared to those of the CVE ($E_{a,SEI} = 31.2 \text{ kJ}$ mol^{-1} and $E_{\text{a,ct}} = 58.3 \text{ kJ mol}^{-1}$). These values of the CVE are consistent with the previously reported studies. 2,5,26,50 Notably, the Li⁺ desolvation energy barrier decreased much in the HSCE, which is known as the most kinetic hindrance process at low-temperature operation of the LIBs. 2,51 These results imply that modified solvation structure and thinner anionderived SEI layer from the HSCE created a more kinetically favorable interface region than that in the CVE for facile electrochemical reactions at low temperature. 5,50 Moreover,

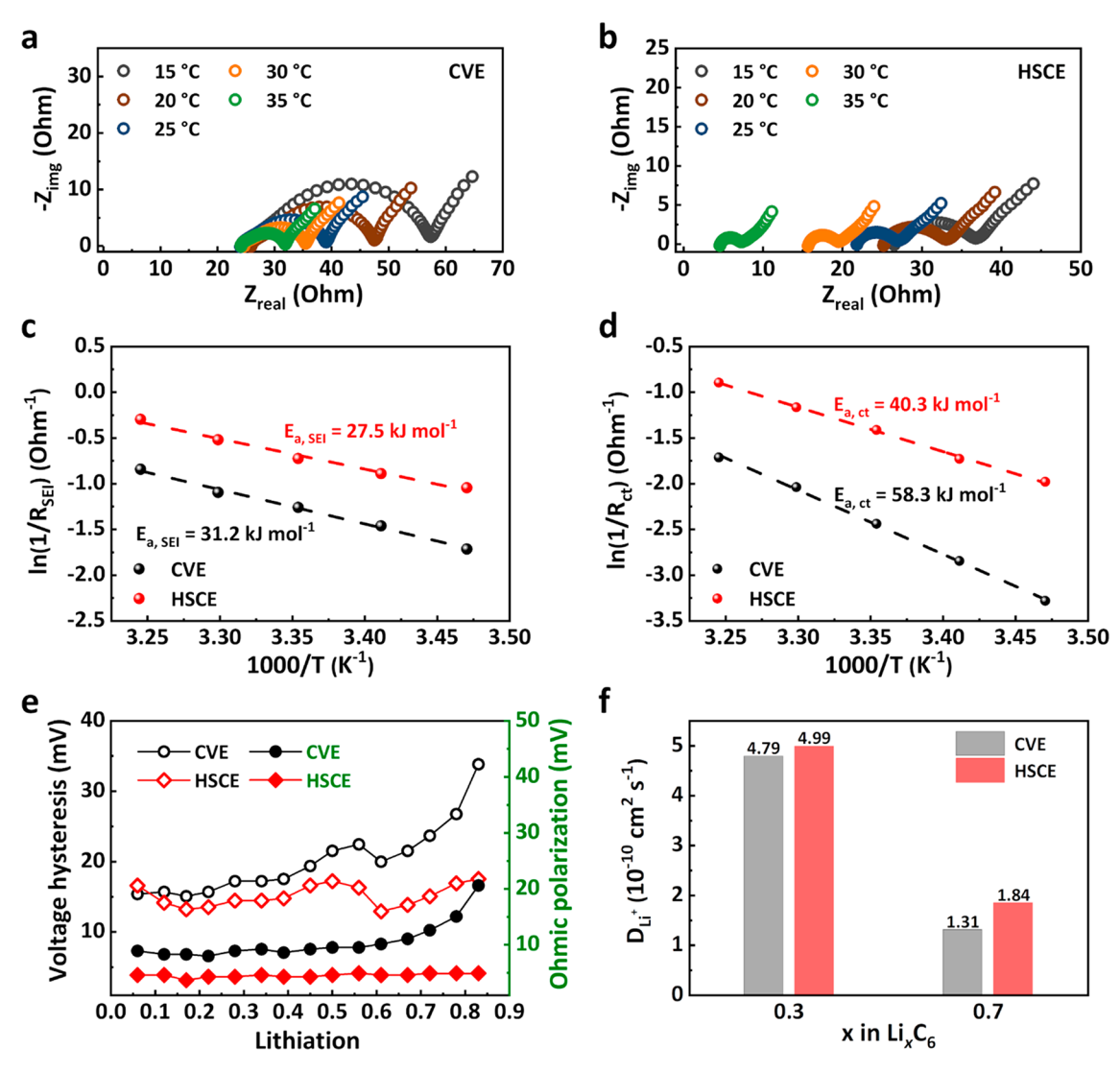


Figure 4. Li⁺ kinetics at the interfacial region and graphite electrodes. Temperature-dependent EIS Nyquist plots of graphite electrodes in (a) CVE and (b) HSCE. Impedance-derived Arrhenius plots for activation energies corresponding to (c) Li⁺ transport through SEI layer and (d) Li⁺ desolvation process. (e) Voltage hysteresis, Ohmic polarization, and (f) Li⁺ diffusion coefficient based on GITT measurement.

significantly improved performance of the graphite electrode at high current rates (5 and 10 C) in the HSCE reinforces the superior Li⁺ reaction kinetics by the HSCE (Figure S18), given that the Li⁺ transport rate at the interfacial region has a strong influence on the performance at high current rate as well.^{2,38}

Galvanostatic intermittent titration technique (GITT) analysis also shows improved Li⁺ diffusion in the HSCE. The voltage hysteresis and Ohmic polarization were lower for the HSCE than CVE especially at high lithiation degree (Figure 4e). This allows facile Li⁺ reactions into the graphite electrode in the HSCE. The resultant lithium diffusion coefficients $(D_{i,i})$ in the graphite electrode, calculated from Figure S19,⁵² were slightly higher in the HSCE $(4.99 \times 10^{-10} \text{ cm}^2 \text{ s}^{-1} \text{ at } x = 0.3)$ and 1.84×10^{-10} cm² s⁻¹ at x = 0.7) than CVE $(4.79 \times 10^{-10}$ cm² s⁻¹ at x = 0.3 and 1.31×10^{-10} cm² s⁻¹ at x = 0.7) (Figure 4f). The efficient SEI in the HSCE may affect the slight increases of the D_{Li^+} . $^{53-55}$ As the higher lability of the HSCE in MD simulations suggests, there was no Li+ transport retardation in the HSCE overall despite its higher viscosity coming from high concentration. Therefore, the HSCE itself and thin anion-derived SEI layer from the HSCE, containing inorganic species with a larger amount of LiF, led to enhanced

overall Li⁺ transport properties without impairing any Li⁺ diffusion process. As a result, the low melting point of THF along with the preferred Li⁺ transport properties of the HSCE boosted the low temperature performance of the LIBs compared with the CVE.

Electrochemical Performance of LiNi_{0.6}Co_{0.2}Mn_{0.2}O₂ (NCM622)||Graphite Full Cells. The newly developed HSCE also enabled full cells composed of the NCM622 cathode and graphite anode to achieve enhanced electrochemical performance at room temperature and low temperatures. The full cells with both electrolytes exhibit similar discharge capacities at the first cycle (CVE: 161.3 mAh g⁻¹; HSCE: 161.0 mAh g⁻¹) and stable cycling performance at room temperature (Figures 5a,b and S20). High salt concentration allowed the THF-based HSCE to have oxidation stability beyond 4.2 V (vs Li/Li⁺) and be compatible with the high-voltage NCM cathode, which otherwise suffered oxidation in the cathode working potential range (Figure S21).¹¹ Moreover, the overpotential during the first charge was much lower in the HSCE due to the improved Li⁺ transport and distinct SEI formation process from the modified solvation structure and anion-derived SEI layer (Figure 5a). This effect

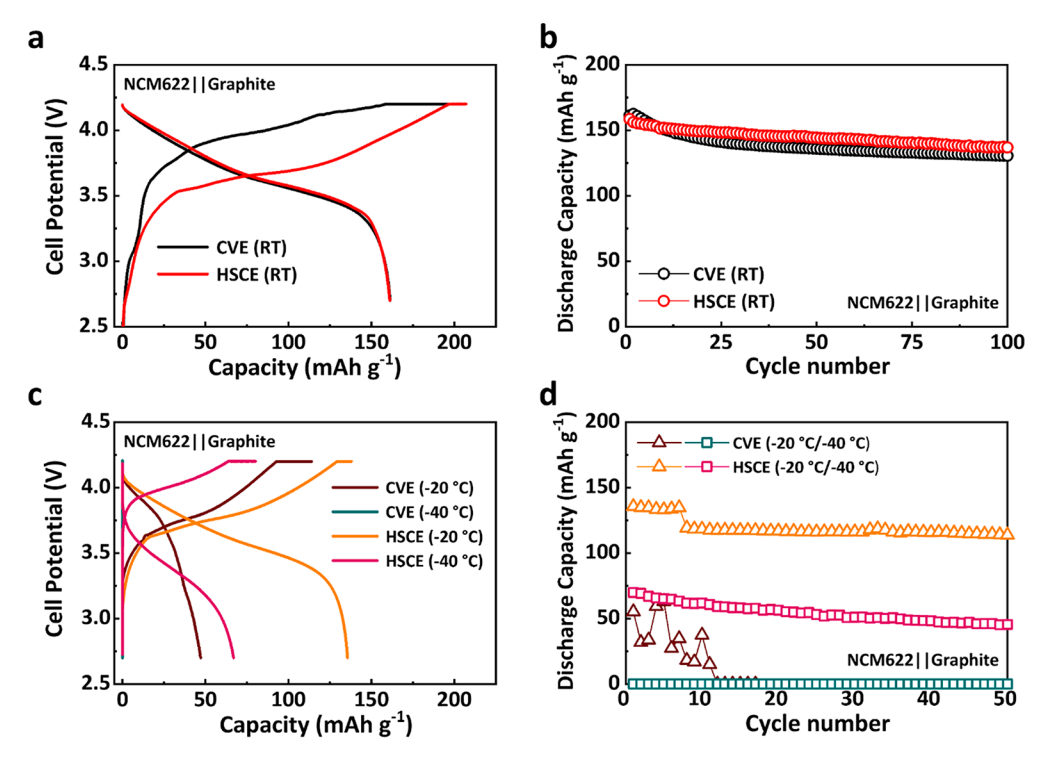


Figure 5. Electrochemical performance of LiNi_{0.6}Co_{0.2}Mn_{0.2}O₂llgraphite full cells. Galvanostatic voltage profiles for (a) the first cycle and (b) cycling performance at 0.2 C (36 mA g⁻¹) and room temperature (RT). (c) Low-temperature galvanostatic voltage profiles and (d) cycling performance at -20 and -40 °C.

was more evident at low temperatures by creating a synergy with the low melting point of THF solvent. At -20 °C, the full cell capacity with the HSCE was over 130 mAh g⁻¹ and maintained over 80% capacity retention of the capacity at room temperature, whereas it was only 50 mAh g⁻¹ and showed severe capacity fluctuation with the CVE (Figure 5c,d). Moreover, even at -40 °C, the full cell with the HSCE shows 70 mAh g⁻¹ (43% capacity retention) (Figure 5c,d). As expected, the capacities decreased at -20 and -40 °C compared to that of at room temperature. However, it generated reasonable electrochemical energy and was rechargeable unlike the full cell with the CVE, which did not function at all at -40 °C.

CONCLUSIONS

In this study, we reported a HSCE electrolyte based on THF:LiFSI with enhanced subzero temperature LIB performance. This design is possible because the HSCE paradigm enables the choice of electrolyte solvent to be decoupled from the quality of the SEI. On the basis of Raman spectra and MD simulations, AGGs are the dominant coordination structure for Li⁺ in these electrolytes. This solvation structure allows relatively labile anion exchange that results in high Li⁺ transference numbers and sustainable Li+ conductivity as the viscosity of the electrolyte increases.

The specific solvation structure of HSCE also contributes to the formation of a thin but robust LiF-rich anion-derived SEI layer that includes various inorganic compounds on the graphitic anode surface of LIB. This SEI layer provided the HSCE with excellent graphite electrode compatibility and highly reversible Li⁺ reactions at room temperature. The enhancement with respect to CVEs became even more apparent in the low-temperature $(0, -20, \text{ and } -40 \text{ }^{\circ}\text{C})$ charge-discharge performance. Furthermore, electrochemical analyses demonstrated that Li⁺ transport properties at the interfacial region were improved without degrading any Li+ diffusion process in LIBs. Overall, the boosted subzero temperature performance can attribute to the low melting point of the HSCE, anion-derived SEI, and distinct Li⁺ transport via AGGs. The enhanced subzero temperature performance was successfully implemented to the full cells composed of NCM622 and graphite electrodes. In conclusion, the HSCE approach provides an avenue for expanding the availability of the LIBs by eliminating the intrinsic limitations of the current LIBs electrolyte system at subzero temperature.

MATERIALS AND METHODS

Materials. Electrolytes were prepared by dissolving a given amount of lithium bis(fluorosulfonyl)imide (LiFSI, TCI America) salts into solvents in an Ar-filled glovebox. Tetrahydrofuran (THF) was purchased from Sigma-Aldrich. All reagents were high purity (>98%) and used without further purification. The molar ratios of LiFSI to THF in the prepared electrolytes are LiFSI-24.6THF (0.5 M), LiFSI-12.3THF (1 M), LiFSI-4.1THF (3 M), and LiFSI-2.5THF (5 M). A conventional electrolyte for comparison is composed of 1.0 M LiPF₆ in a mixture of ethylene carbonate (EC) and diethyl carbonate (DEC) (Sigma-Aldrich, 1:1 v/v, battery grade).

Structural Characterization. Coordination structures of solutions were identified by a Raman microscope (Thermo Scientific DXR 2) with a 613 nm laser. TEM analyses and EDS chemical mapping were performed on a transmission electron microscope (Thermo Scientific FEI Talos 200X) operated at 200 kV equipped with a high angle annular dark field (HAADF) detector and SuperX EDS with four silicon drift detectors. All the EDS maps were captured under the drift correction mode. Surface chemistries of graphite electrodes were investigated by an X-ray photoelectron spectrometer (Kratos AXIS Ultra) equipped with a monochromatized Al K α X-ray source. The electrodes were cycled 10 times for SEI formation and washed with dimethyl carbonate (DMC) in the Ar-filled glovebox to remove residual electrolyte components before TEM and XPS

analyses. Viscosities of electrolytes were measured by a rheometer (TA Instruments DHR-3) at 25 °C.

Molecular Dynamics Simulations. All molecular dynamics simulations were performed with the LAMMPS package. For each condition, three independent trajectories of 100 ns have been obtained by using a 1 fs time step. The last 10 ns of these trajectories has been used for the analyses to ensure that well-equilibrated configurations are obtained. Dynamic properties of electrolytes including viscosities and conductivities are known to be difficult to predict by using classical force fields due to polarization effects. 56, To describe Li⁺ electrolyte systems with classical force fields, the atomic partial charges are often rescaled by a factor of 0.7-0.8 to account for the polarization effects by mimicking the average charge screening due to polarization. Sensitivity analysis (Figure S1) shows that the charge rescaling by a factor of 0.8 provided conductivities and transference numbers that are in good agreement with the reported experimental values.⁴⁰ Further details are described in the Supporting Information.

Electrochemical Measurements. The graphite electrodes consisting of mesocarbon microbeads (MCMB) graphite (91.83 wt %) as an active material, C45 (2 wt %) as a conductive agent, poly(vinylidene difluoride) (PVDF) (6 wt %) as a binder, and oxalic acid (0.17 wt %) as an additive were prepared onto Cu foil with a mass loading of 6.2-6.3 mg cm⁻² (CAMP Facility at Argonne National Laboratory (ANL)). Half-cells were assembled by using CR2032 coin-type cells with lithium metal as a counter electrode, a polypropylene membrane (Celgard 2500) as a separator, and the prepared electrolytes in the Ar-filled glovebox. The half-cell galvanostatic charge/discharge measurement was performed by using a battery-testing system (Arbin BT-2000) at a voltage range of 0.01-1.5 V versus Li/Li⁺. Charging (lithiation) was performed in a constant current-constant voltage mode, and discharging (delithiation) was performed in a constant current mode. To determine cycling stability at room temperature, the half-cells were cycled at a 0.5 C-rate (1 C = 372 mA g^{-1}). For low-temperature performance tests, the half-cells were charged and discharged with the following Crate at several temperatures (0.1 C/0.2 C for 0 °C, 0.1 C/0.1 C for -20 °C, and 0.05 C/0.05 C for -40 °C). Formation cycles were given for the cells at 0.1 C-rate for five cycles before all cycling tests. Rate capability tests were performed with different current rates (0.2-10 C) at room temperature.

Cyclic voltammetry (CV), electrochemical impedance spectroscopy (EIS), DC polarization, and linear sweep voltammetry (LSV) measurements were performed by using a potentiostat (Gamry Reference 600+). The CV tests for the graphite half-cells were conducted in the potential range between 0.01 and 1.5 V (vs Li/Li⁺) at a scan rate of 0.1 mV s-1. The transference numbers of the electrolytes were determined through the potentiostatic polarization method with LillLi symmetric cells at room temperature. 48 The following equation is utilized to calculate the transference number:

$$t_{+} = \frac{I_{SS}(\Delta V - I_{0}R_{0})}{I_{0}(\Delta V - I_{SS}R_{SS})}$$

The EIS was performed over a frequency range of 1 MHz-10 mHz with 10 mV amplitude of AC voltage perturbation before and after DC polarization to obtain the initial cell impedance (R_0) and steadystate cell impedance (R_{SS}). The DC polarization was applied with a constant voltage of 10 mV (ΔV) for 4000 s to obtain the initial current (I_0) and steady-state current (I_{SS}) . The EIS for the activation energy measurement was performed over a frequency range of 1 MHz-10 mHz with 10 mV amplitude of AC voltage perturbation at several temperatures (15–35 °C). Before the EIS, the half-cells were cycled at 0.1 C for five cycles to complete SEI formation and held at 0.15~V until the current reaches 0.01~C, which is the characteristic Li^+ intercalation potential of the graphite. The LSV was conducted with the Al working electrode and Li reference and counter electrodes, sweeping from open circuit potential to 5.5 V at a rate of 0.5 mV s⁻¹. Ionic conductivities of the electrolytes were measured by a temperature-controlled electrochemical cell system (Autolab Microcell HC with TSC 1600 cell) between -20 and 40 °C with temperature increments of 10 °C. Galvanostatic intermittent titration technique (GITT) measurement for the half-cells was performed by using the battery-testing system (Arbin BT-2000) with 0.2 C of pulse current density for 0.5 h followed by 2 h of equilibration time.

For coin-type full cells, the stated graphite and LiNi_{0.6}Co_{0.2}Mn_{0.2}O₂ (NCM622) electrodes were employed with an N/P ratio (capacity ratio of negative to positive electrode) of 1.30-1.35. The NCM622 electrodes composed of NCM622 (90 wt %) as an active material, C45 (5 wt %) as a conductive agent, and PVDF (5 wt %) as a binder were coated on Al foil with a mass loading of 9.4-9.7 mg cm⁻² (CAMP Facility at ANL). The full cells were fabricated employing CR2032 coin-type cells with a polypropylene membrane (Celgard 2500) as a separator and the prepared electrolytes in the Ar-filled glovebox. For galvanostatic charge-discharge tests of the coin-type full cells, the cells were charged by using constant current constant voltage mode and discharged by using constant current mode within the voltage range of 2.7-4.2 V. The cells were charged and discharged with the following C-rate (1 C = 180 mA g^{-1}) at several temperatures (0.2 C/0.2 C for room temperature, 0.05 C/0.05 C for -20 °C, and 0.025 C/0.025 C for $-40 \,^{\circ}\text{C}$). Formation cycles were carried out for the cells at 0.2 C-rate for five cycles at room temperature before low temperatures (-20 and -40 °C) full cell cycling.

ASSOCIATED CONTENT

Supporting Information

The Supporting Information is available free of charge at https://pubs.acs.org/doi/10.1021/acsami.2c09338.

MD simulations; XPS data; EIS curve fitting; TEM images; cyclic voltammetry curves; charge-discharge profiles; viscosities; ionic conductivities; Li⁺ transference numbers; Coulombic efficiencies; linear sweep voltammetry curves (PDF)

AUTHOR INFORMATION

Corresponding Authors

Brett M. Savoie - Davidson School of Chemical Engineering, Purdue University, West Lafayette, Indiana 47907, United *States;* orcid.org/0000-0002-7039-4039;

Email: bsavoie@purdue.edu

Vilas G. Pol – Davidson School of Chemical Engineering, Purdue University, West Lafayette, Indiana 47907, United States; o orcid.org/0000-0002-4866-117X; Email: vpol@ purdue.edu

Authors

Soohwan Kim - Davidson School of Chemical Engineering, Purdue University, West Lafayette, Indiana 47907, United States; orcid.org/0000-0003-1290-5539

Bumjoon Seo - Davidson School of Chemical Engineering, Purdue University, West Lafayette, Indiana 47907, United States; orcid.org/0000-0002-5029-1593

Hari Vignesh Ramasamy - Davidson School of Chemical Engineering, Purdue University, West Lafayette, Indiana 47907, United States; orcid.org/0000-0002-8241-2441

Zhongxia Shang - School of Materials Engineering, Purdue University, West Lafayette, Indiana 47907, United States Haiyan Wang – School of Materials Engineering, Purdue University, West Lafayette, Indiana 47907, United States; orcid.org/0000-0002-7397-1209

Complete contact information is available at: https://pubs.acs.org/10.1021/acsami.2c09338

Author Contributions

S.K. and B.S. contributed equally to this work. S.K. and V.G.P. conceived the idea. S.K. conducted the materials synthesis, materials characterizations, electrochemical testing, and data analysis. B.S. and B.M.S. performed molecular simulations. Z.S. and H.W. performed TEM analysis. S.K. and B.S. wrote the manuscript. H.V.R., B.M.S., and V.G.P. reviewed and edited the manuscript. V.G.P. supervised this work.

Notes

The authors declare no competing financial interest.

ACKNOWLEDGMENTS

V.G.P. truly thanks the financial support from the Naval Enterprise Partnership Teaming with Universities for National Excellence (NEPTUNE), Office of Naval Research (Grant # N000142112070), and the Program Manager, Maria Medeiros. The electrodes were produced at the U.S. Department of Energy's (DOE) CAMP (Cell Analysis, Modeling and Prototyping) Facility, Argonne National Laboratory. The CAMP Facility is fully supported by the DOE Vehicle Technologies Office (VTO). A provisional US patent (PRF # 2022-POL-69515) has been filed by Dr. D. H. R. Sarma, Registered USPTO Patent Practitioner, of the Purdue Research Foundation, IN, USA, on the experimental research work displayed in this manuscript. The XPS data were obtained at the Materials Research Laboratory Central Research Facilities in University of Illinois Urbana-Champaign. Z.S. and H.W. acknowledge the financial support from the U.S. Office of Naval Research (N00014-20-1-2043) for the TEM effort.

REFERENCES

- (1) Goodenough, J. B.; Park, K. S. The Li-ion Rechargeable Battery: A Perspective. J. Am. Chem. Soc. 2013, 135, 1167-1176.
- (2) Cai, W.; Yao, Y. X.; Zhu, G. L.; Yan, C.; Jiang, L. L.; He, C.; Huang, J. Q.; Zhang, Q. A Review on Energy Chemistry of Fast-Charging Anodes. Chem. Soc. Rev. 2020, 49, 3806-3833.
- (3) Gupta, A.; Manthiram, A. Designing Advanced Lithium-based Batteries for Low-Temperature Conditions. Adv. Energy Mater. 2020, 10, 2001972.
- (4) Hou, J.; Yang, M.; Wang, D.; Zhang, J. Fundamentals and Challenges of Lithium Ion Batteries at Temperatures between - 40 and 60 °C. Adv. Energy Mater. 2020, 10, 1904152.
- (5) Xu, K.; Lam, Y.; Zhang, S. S.; Jow, T. R.; Curtis, T. B. Solvation Sheath of Li⁺ in Nonaqueous Electrolytes and Its Implication of Graphite/Electrolyte Interface Chemistry. J. Phys. Chem. C 2007, 111, 7411-7421.
- (6) Li, Q.; Lu, D.; Zheng, J.; Jiao, S.; Luo, L.; Wang, C. M.; Xu, K.; Zhang, J. G.; Xu, W. Li⁺-Desolvation Dictating Lithium-ion Battery's Low-Temperature Performances. ACS Appl. Mater. Interfaces 2017, 9, 42761-42768.
- (7) Li, Q.; Jiao, S.; Luo, L.; Ding, M. S.; Zheng, J.; Cartmell, S. S.; Wang, C. M.; Xu, K.; Zhang, J. G.; Xu, W. Wide-Temperature Electrolytes for Lithium-ion Batteries. ACS Appl. Mater. Interfaces 2017, 9, 18826-18835.
- (8) Xu, K. Nonaqueous Liquid Electrolytes for Lithium-based Rechargeable Batteries. Chem. Rev. 2004, 104, 4303-4417.
- (9) Jaguemont, J.; Boulon, L.; Dubé, Y. A Comprehensive Review of Lithium-ion Batteries Used in Hybrid and Electric Vehicles at Cold Temperatures. Appl. Energy 2016, 164, 99-114.
- (10) Zheng, J.; Lochala, J. A.; Kwok, A.; Deng, Z. D.; Xiao, J. Research Progress towards Understanding the Unique Interfaces between Concentrated Electrolytes and Electrodes for Energy Storage Applications. Adv. Sci. 2017, 4, 1700032.

- (11) Yamada, Y.; Wang, J.; Ko, S.; Watanabe, E.; Yamada, A. Advances and Issues in Developing Salt-Concentrated Battery Electrolytes. Nat. Energy 2019, 4, 269-280.
- (12) Li, M.; Wang, C.; Chen, Z.; Xu, K.; Lu, J. New Concepts in Electrolytes. Chem. Rev. 2020, 120, 6783-6819.
- (13) Henderson, W. A. Glyme-Lithium Salt Phase Behavior. J. Phys. Chem. B 2006, 110, 13177-13183.
- (14) Yan, C.; Jiang, L. L.; Yao, Y. X.; Lu, Y.; Huang, J. Q.; Zhang, Q. Nucleation and Growth Mechanism of Anion-derived Solid Electrolyte Interphase in Rechargeable Batteries. Angew. Chem., Int. Ed. 2021, 60, 8521-8525.
- (15) Wang, Z.; Qi, F.; Yin, L.; Shi, Y.; Sun, C.; An, B.; Cheng, H. M.; Li, F. An Anion-Tuned Solid Electrolyte Interphase with Fast Ion Transfer Kinetics for Stable Lithium Anodes. Adv. Energy Mater. 2020,
- (16) Yao, Y. X.; Yan, C.; Zhang, Q. Emerging Interfacial Chemistry of Graphite Anodes in Lithium-ion Batteries. Chem. Commun. 2020, 56, 14570-14584.
- (17) Yamada, Y.; Yaegashi, M.; Abe, T.; Yamada, A. A Superconcentrated Ether Electrolyte for Fast-Charging Li-ion Batteries. Chem. Commun. 2013, 49, 11194-11196.
- (18) Yamada, Y.; Furukawa, K.; Sodeyama, K.; Kikuchi, K.; Yaegashi, M.; Tateyama, Y.; Yamada, A. Unusual Stability of Acetonitrile-based Superconcentrated Electrolytes for Fast-Charging Lithium-ion Batteries. J. Am. Chem. Soc. 2014, 136, 5039-5046.
- (19) Alvarado, J.; Schroeder, M. A.; Zhang, M.; Borodin, O.; Gobrogge, E.; Olguin, M.; Ding, M. S.; Gobet, M.; Greenbaum, S.; Meng, Y. S.; Xu, K. A Carbonate-free, Sulfone-based Electrolyte for High-Voltage Li-ion Batteries. Mater. Today 2018, 21, 341-353.
- (20) Moon, H.; Tatara, R.; Mandai, T.; Ueno, K.; Yoshida, K.; Tachikawa, N.; Yasuda, T.; Dokko, K.; Watanabe, M. Mechanism of Li Ion Desolvation at the Interface of Graphite Electrode and Glyme-Li Salt Solvate Ionic Liquids. J. Phys. Chem. C 2014, 118, 20246-
- (21) Lu, D.; Tao, J.; Yan, P.; Henderson, W. A.; Li, Q.; Shao, Y.; Helm, M. L.; Borodin, O.; Graff, G. L.; Polzin, B.; Wang, C. M.; Engelhard, M.; Zhang, J. G.; De Yoreo, J. J.; Liu, J.; Xiao, J. Formation of Reversible Solid Electrolyte Interface on Graphite Surface from Concentrated Electrolytes. Nano Lett. 2017, 17, 1602-1609.
- (22) Abraham, K. M.; Goldman, J. L. The Use of the Reactive Ether, Tetrahydrofuran (THF), in Rechargeable Lithium Cells. J. Power Sources 1983, 9, 239-245.
- (23) Abraham, K. M.; Pasquariello, D. M.; Martin, F. J. Mixed Ether Electrolytes for Secondary Lithium Batteries with Improved Low Temperature Performance. J. Electrochem. Soc. 1986, 133, 661-666.
- (24) Cheng, P.; Zhang, H.; Ma, Q.; Feng, W.; Yu, H.; Huang, X.; Armand, M.; Zhou, Z. Highly Salt-Concentrated Electrolyte Comprising Lithium Bis(fluorosulfonyl)imide and 1,3-Dioxolanebased Ether Solvents for 4-V-class Rechargeable Lithium Metal Cell. Electrochim. Acta 2020, 363, 137198.
- (25) Zhang, N.; Sun, C.; Huang, Y.; Zhu, C.; Wu, Z.; Lv, L.; Zhou, X.; Wang, X.; Xiao, X.; Fan, X.; Chen, L. Tuning Electrolyte Enables Microsized Sn as an Advanced Anode for Li-ion Batteries. J. Mater. Chem. A 2021, 9, 1812-1821.
- (26) Yao, Y. X.; Chen, X.; Yan, C.; Zhang, X. Q.; Cai, W. L.; Huang, J. Q.; Zhang, Q. Regulating Interfacial Chemistry in Lithium-ion Batteries by a Weakly Solvating Electrolyte. Angew. Chem., Int. Ed. 2021, 60, 4090-4097.
- (27) Chen, J.; Fan, X.; Li, Q.; Yang, H.; Khoshi, M. R.; Xu, Y.; Hwang, S.; Chen, L.; Ji, X.; Yang, C.; He, H.; Wang, C.; Garfunkel, E.; Su, D.; Borodin, O.; Wang, C. Electrolyte Design for LiF-rich Solid-Electrolyte Interfaces to Enable High-Performance Microsized Alloy Anodes for Batteries. Nat. Energy 2020, 5, 386-397.
- (28) Borodin, O.; Gorecki, W.; Smith, G. D.; Armand, M. Molecular Dynamics Simulation and Pulsed-field Gradient NMR Studies of Bis(fluorosulfonyl)imide (FSI) and Bis[(trifluoromethyl)sulfonyl]imide (TFSI)-based Ionic Liquids. J. Phys. Chem. B 2010, 114, 6786-6798.

- (29) Tsuzuki, S.; Hayamizu, K.; Seki, S. Origin of the Low-Viscosity of [emim][(FSO₂)₂N] Ionic Liquid and Its Lithium Salt Mixture: Experimental and Theoretical Study of Self-Diffusion Coefficients, Conductivities, and Intermolecular Interactions. J. Phys. Chem. B 2010, 114, 16329-16336.
- (30) Xu, K. Electrolytes and Interphases in Li-ion Batteries and Beyond. Chem. Rev. 2014, 114, 11503-11618.
- (31) Fan, X.; Chen, L.; Ji, X.; Deng, T.; Hou, S.; Chen, J.; Zheng, J.; Wang, F.; Jiang, J.; Xu, K.; Wang, C. Highly Fluorinated Interphases Enable High-Voltage Li-Metal Batteries. Chem. 2018, 4, 174–185.
- (32) Zheng, X.; Huang, L.; Luo, W.; Wang, H.; Dai, Y.; Liu, X.; Wang, Z.; Zheng, H.; Huang, Y. Tailoring Electrolyte Solvation Chemistry toward an Inorganic-Rich Solid-Electrolyte Interphase at a Li Metal Anode. ACS Energy Lett. 2021, 6, 2054-2063.
- (33) Ugata, Y.; Tatara, R.; Mandai, T.; Ueno, K.; Watanabe, M.; Dokko, K. Understanding the Reductive Decomposition of Highly Concentrated Li Salt/Sulfolane Electrolytes during Li Deposition and Dissolution. ACS Appl. Energy Mater. 2021, 4, 1851-1859.
- (34) Kumar, A.; Kumar, R.; Linga, P. Sodium Dodecyl Sulfate Preferentially Promotes Enclathration of Methane in Mixed Methane-Tetrahydrofuran Hydrates. iScience 2019, 14, 136-146.
- (35) Li, H.; Stanwix, P.; Aman, Z.; Johns, M.; May, E.; Wang, L. Raman Spectroscopic Studies of Clathrate Hydrate Formation in the Presence of Hydrophobized Particles. J. Phys. Chem. A 2016, 120, 417-424.
- (36) Ojha, A. K.; Srivastava, S. K.; Peica, N.; Schlücker, S.; Kiefer, W.; Asthana, B. P. Concentration Dependent Wavenumber Shifts and Linewidth Changes of Some Prominent Vibrational Modes of C₄H₈O Investigated in a Binary System (C₄H₈O+H₂O) by Polarized Raman Study and Ab initio Calculations. J. Mol. Struct. 2005, 735-736, 349-
- (37) Fawdon, J.; Ihli, J.; Mantia, F.; Pasta, M. Characterising Lithium-ion Electrolytes via Operando Raman Microspectroscopy. Nat. Commun. 2021, 12, 4053.
- (38) Jiang, L. L.; Yan, C.; Yao, Y. X.; Cai, W.; Huang, J. Q.; Zhang, Q. Inhibiting Solvent Co-Intercalation in a Graphite Anode by a Localized High-Concentration Electrolyte in Fast-Charging Batteries. Angew. Chem., Int. Ed. 2021, 60, 3402-3406.
- (39) Savoie, B. M.; Webb, M. A.; Miller, T. F., III Enhancing Cation Diffusion and Suppressing Anion Diffusion via Lewis-Acidic Polymer Electrolytes. J. Phys. Chem. Lett. 2017, 8, 641-646.
- (40) Pham, T. D.; Bin Faheem, A.; Lee, K. K. Design of a LiF-rich Solid Electrolyte Interphase Layer through Highly Concentrated LiFSI-THF Electrolyte for Stable Lithium Metal Batteries. Small 2021, 17, 2103375.
- (41) Cao, X.; Xu, Y.; Zhang, L.; Engelhard, M. H.; Zhong, L.; Ren, X.; Jia, H.; Liu, B.; Niu, C.; Matthews, B. E.; Wu, H.; Arey, B. W.; Wang, C.; Zhang, J. G.; Xu, W. Nonflammable Electrolytes for Lithium Ion Batteries Enabled by Ultraconformal Passivation Interphases. ACS Energy Lett. 2019, 4, 2529-2534.
- (42) He, M.; Guo, R.; Hobold, G. M.; Gao, H.; Gallant, B. M. The Intrinsic Behavior of Lithium Fluoride in Solid Electrolyte Interphases on Lithium. Proc. Natl. Acad. Sci. U. S. A. 2020, 117, 73-79.
- (43) Qu, J.; Meyer, III, H. M. X-Ray Photoelectron Spectroscopy (XPS). In Encyclopedia of Tribology; Wang, Q. J., Chung, Y.-W., Eds.; Springer: 2013; pp 4133-4138.
- (44) Yan, C.; Xu, R.; Xiao, Y.; Ding, J. F.; Xu, L.; Li, B. Q.; Huang, J. Q. Toward Critical Electrode/Electrolyte Interfaces in Rechargeable Batteries. Adv. Funct. Mater. 2020, 30, 1909887.
- (45) Liu, T.; Lin, L.; Bi, X.; Tian, L.; Yang, K.; Liu, J.; Li, M.; Chen, Z.; Lu, J.; Amine, K.; Xu, K.; Pan, F. In situ Quantification of Interphasial Chemistry in Li-ion Battery. Nat. Nanotechnol. 2019, 14, 50-56.
- (46) An, S. J.; Li, J.; Daniel, C.; Mohanty, D.; Nagpure, S.; Wood, D. L., III The State of Understanding of the Lithium-ion-Battery Graphite Solid Electrolyte Interphase (SEI) and Its Relationship to Formation Cycling. Carbon 2016, 105, 52-76.
- (47) Buss, H. G.; Chan, S. Y.; Lynd, N. A.; McCloskey, B. D. Nonaqueous Polyelectrolyte Solutions as Liquid Electrolytes with

- High Lithium Ion Transference Number and Conductivity. ACS Energy Lett. 2017, 2, 481-487.
- (48) Zugmann, S.; Fleischmann, M.; Amereller, M.; Gschwind, R. M.; Wiemhöfer, H. D.; Gores, H. J. Measurement of Transference Numbers for Lithium Ion Electrolytes via Four Different Methods, A Comparative Study. Electrochim. Acta 2011, 56, 3926-3933.
- (49) Diederichsen, K. M.; McShane, E. J.; McCloskey, B. D. Promising Routes to a High Li⁺ Transference Number Electrolyte for Lithium Ion Batteries. ACS Energy Lett. 2017, 2, 2563-2575.
- (50) Xu, K. Charge-Transfer" Process at Graphite/Electrolyte Interface and the Solvation Sheath Structure of Li⁺ in Nonaqueous Electrolytes. J. Electrochem. Soc. 2007, 154, A162-A167.
- (51) Xu, K.; von Wald Cresce, A. Li⁺-Solvation/Desolvation Dictates Interphasial Processes on Graphitic Anode in Li Ion Cells. J. Mater. Res. 2012, 27, 2327-2341.
- (52) Weppner, W.; Huggins, R. A. Determination of the Kinetic Parameters of Mixed Conducting Electrodes and Application to the System Li₃Sb. J. Electrochem. Soc. 1977, 124, 1569-1578.
- (53) Fang, J.-B.; Chang, S.; Ren, Q.; Zi, T.; Wu, D.; Li, A.-D. Tailoring Stress and Ion-Transport Kinetics via a Molecular Layer Deposition-Induced Artificial Solid Electrolyte Interphase for Durable Silicon Composite Anodes. ACS Appl. Energy Mater. 2021, 13, 32520-32530.
- (54) Rangom, Y.; Duignan, T. T.; Zhao, X. S. Lithium-Ion Transport Behavior in Thin-Film Graphite Electrodes with SEI Layers Formed at Different Current Densities. ACS Appl. Energy Mater. 2021, 13, 42662-42669.
- (55) Wang, C.; Sun, X.; Zhang, X.; Li, H. Introducing Nanodiamonds in Electrolyte and SEI for Highly Improving Performances of Lithium-ion Batteries. Appl. Surf. Sci. 2022, 600, 154178.
- (56) Doherty, B.; Zhong, X.; Gathiaka, S.; Li, B.; Acevedo, O. Revisiting OPLS Force Field Parameters for Ionic Liquid Simulations. J. Chem. Theory Comput. 2017, 13, 6131-6145.
- (57) Borodin, O. Polarizable Force Field Development and Molecular Dynamics Simulations of Ionic Liquids. J. Phys. Chem. B 2009, 113, 11463-11478.
- (58) Park, C.; Kanduč, M.; Chudoba, R.; Ronneburg, A.; Risse, S.; Ballauff, M.; Dzubiella, J. Molecular Simulations of Electrolyte Structure and Dynamics in Lithium-Sulfur Battery Solvents. J. Power Sources 2018, 373, 70-78.
- (59) Li, Z.; Bouchal, R.; Mendez-Morales, T.; Rollet, A. L.; Rizzi, C.; Le Vot, S.; Favier, F.; Rotenberg, B.; Borodin, O.; Fontaine, O.; Salanne, M. Transport Properties of Li-TFSI Water-in-Salt Electrolytes. J. Phys. Chem. B 2019, 123, 10514-10521.